Bioimage Informatics For Plant Sciences

Blobs and Curves: Object-Based Colocalisation for Plant Cells

Carl J. Nelson (A), Patrick Duckney, (B), Timothy J. Hawkins (B), Michael J. Deeks (C), P. Philippe Laissue (D), Patrick J. Hussey (B) and Boguslaw Obara (A)(*)

(A) School of Engineering and Computing Sciences, Durham University, Durham, UK
(B) School of Biological and Biomedical Sciences, Durham University, Durham, UK
(C) College of Life and Environmental Sciences, University of Exeter, Exeter, UK
(D) School of Biological Sciences, University of Essex, Colchester, UK
(*) Corresponding author (email: boguslaw.obara@dur.ac.uk)

Abstract: Quantifying the colocalisation of labels is a major application of fluorescent microscopy in plant biology. Pixel-based quantification of colocalisation, such as Pearson's correlation coefficient, gives limited information for further analysis. We show how applying bioimage informatics tools to a commonplace experiment allows further quantifiable results to be extracted. We use our object-based colocalisation technique to extract distance information, show temporal changes and demonstrate the advantages, and pitfalls, of using bioimage informatics for plant science.

Keywords: Bioimage Informatics, Colocalisation, Plant Science, Actin-Binding Proteins, Mitochondrial Trafficking, Image Analysis, Fluorescence Microscopy.

Introduction

In the past twenty years a revolution in plant science has occurred: the age of genomics. From the development of genome sequencing technologies to the bioinformatics tools used to store, manage and analyse the data (see Yang et al. 2013 for a recent example of the tools available), a whole new interdisciplinary field of research has emerged, supported by accessible tools and dedicated international journals. Unfortunately with this "gold-rush" of genomic tools, techniques and understanding, a classic tool of biology has been left behind: phenotyping. Phenotypic analysis has been essential from the days of Mendel but is now considered the bottleneck of high-throughput biological sciences (Cobb et al. 2013). A lack of automation of phenotype analysis and indeed a lack of investment in necessary programming skills within the plant science community are slowing an informatics-driven enlightenment.

With the advent of digital imaging and ever more powerful computers, microscopy as a tool for phenotyping has moved from qualitative observation to quantitative analysis of biological samples and assays (see Thomasson and Macnaughtan (2013) for review). Exciting developments in the world of microscopy (see Sappl and Heisler (2013) for review) have brought about a dramatic increase in spatial and temporal resolution, producing massive image files that hold a great amount of data. Enter

bioimage informatics, an area where biological study, bioimaging methods and computer vision analysis meet to manage and analyse data from a wide variety of experiments (Swedlow et al. 2003).

In plant sciences, this alliance is often hidden under the term phenotyping and the term image analysis only mentioned when explicit computational methods are used (e.g. Cobb et al. 2013); this can lead to problems of reproducibility and comparison of results (Cardona and Tomancak 2012). In this paper, we will outline the state of bioimage informatics in plant sciences before showcasing two examples of fluorescence colocalisation. These examples show how bioimage informatics technology can be applied across experiments and systems and also highlight possible pitfalls in designing and using bioimage informatics tools.

Bioimage Informatics in the Plant Sciences

Although the term bioimage informatics is often used in relation to cellular and molecular biology, it is primarily the management, analysis and storage of large scale data sets from images within the life sciences (see Eliceiri et al. (2012) for a review of computational involvement in imaging and optical technologies). In plant sciences this can encompass anything from the canopies of forests to the colocalisation of protein signals within leaf cells. Many bioimage informatics tools are, of course, transferable across all of the biological sciences, such examples include the Open Microscopy Environment Remote Objects (OMERO; Allan et al. 2012) and Bio-Image Semantic Query User Environment (Bisque; Kvilekval et al. 2010) platforms, an open-source management and access software for a wide range of biological data. Indeed new features are being developed that add functionality to such systems (e.g. Cho et al. 2012).

More specifically to plant sciences, there are now collaborative groups, such as the iPlant Collaborative (Goff et al. 2011), aiming to develop 'cyberinfrastructure and computational tools' within plant sciences. Such groups aim to help collaboration and development of a wide range of high-quality tools for analysis, inference, management and prediction amongst plant scientists. Further, online collections of bioimage informatics tools are being created to help plant scientists find the appropriate tools without having to sift through a plentitude of academic journals (Lobet et al. 2013).

Lobet and co-workers (Lobet et al. 2013) show that their database has software that performs bioimage informatics from the canopy level through leaf, root and shoot right through to cellular analysis. Algorithms range from cell wall segmentation (Roeder et al. 2010) and cell tracing (Lichius et al. 2013) to leaf disease identification, species identification, root network mapping and canopy coverage. Network extraction methods are particularly popular, from extraction of fungal networks (Obara et al. 2012), to connected plant cell walls (Pound et al. 2012) and leaf venation (Dhondt et al. 2012; Rolland-Lagan et al. 2009). Such network extraction systems can often be adjusted for different scales, and applied to macroscopic fungal or root networks as well as subcellular filament networks (Fichtl et al. 2011).

Challenges in Bioimage Informatics

Many available bioimage informatics softwares give similar measurements as their final outcome but it is up to the individual experimenter to discover which algorithm produces the most reliable results for

their own experimental data: it is often the case that one program is more suited to one modality or one scenario. Scientists in biological labs require software solutions that are tailored to their specific needs and collaborations with computer scientists can often be the most efficient way forward in developing new tools. These tools should be well documented, such that the developed algorithm and approach can be replicated and understood by those trying to validate or contest the results of the experiments (Pridmore et al. 2012).

From the computer science perspective there are also the challenges of developing user-friendly software, while still maintaining a scientific openness within the code. The challenges regarding bioimage informatics software usability have recently been reviewed, identifying many different criteria (Carpenter et al. 2012). These criteria include not just user-friendliness, but also the ability to adapt the software for new uses; the interoperability of the software, i.e. the ability to use different languages, operating systems, file formats and data formats; and the validation of the software at different levels.

Validation of software is particularly important. If an experimental scientist takes to using a particular set of computational tools, that scientist must be aware of how the tools have been validated and whether the criteria assumed for that validation hold true for this experiment's data (Pridmore et al. 2012). To aid such validation, new tools are being developed in the bioimage informatics sphere with repositories of synthetic images (e.g. Rajaramet al. 2012), fully annotated images (e.g. Ljosa et al. 2013) or segmentation benchmark infrastructures (e.g. Gelasca et al. 2009).

Colocalisation of NET1A with Plasmodesmata

Plasmodesmata are the numerous channels that provide routes of intercellular transport and communication between the cells of multicellular plants. Retraction of the plasma membrane caused by osmotic shock can reveal their presence through the pinched strands of the protoplast running through their centre, thus making them visible to early botanical microscopists. In the root meristem of *Arabidopsis thaliana*, plasmodesmata are only 30 nm in diameter, yet accommodate a complex membrane-bound structure of protein scaffolds and tubular endoplasmic reticulum. Assignment of protein localisation to plasmodesmata using fluorescence microscopy is achieved using co-labelling with either antibodies or fusions to known plasmodesmal components; or the staining of plasmodesmal-associated callose in the surrounding cell wall (e.g. Deeks et al. 2012). At standard optical resolution the location of callose accumulation is often indistinguishable from the plasmodesmal mouth and channel (e.g. Deeks et al. 2012). The majority of publications demonstrating positive colocalisation between known pore components and uncharacterised proteins use transient expression assays in plant tissues where plasmodesmata exist as isolated and distinctive entities; for this reason, complex colocalisation analysis is not required. In tissues such as the *A. thaliana* root meristem the pattern of plasmodesmata is condensed, with neighbouring pores clustering at distances close to the diffraction limit of resolution (e.g. Simpson et al. 2009; Deeks et al. 2012). The segregation of root meristem cell boundaries into distinctive nano-domains of protein localisation not necessarily connected to plasmodesmal distribution (Kleine-Vehn et al. 2011) further complicates analysis.

In this study we re-analyse a published colocalisation study of the actin-binding protein NET1A-GFP with labelled root meristem plasmodesmata (Deeks et al. 2012) using object-based algorithms. We show that this method provides a quantified overview of the spatial relationship between NET1A-GFP fusion protein and aniline blue signals in units of distance rather than an abstract coefficient. We also demonstrate that this method is effective at removing the influence of background signal inherent to deep-tissue plant fluorescence microscopy.

Colocalisation of Mitochondria with Actin Filaments

The pollen tube is a model example of anisotropic plant cell expansion, in which growth occurs only at the tip (Hepler et al. 2001). Polarised growth is dependent on the tightly regulated spatiotemporal coordination of the pollen tube growth machinery by the actin cytoskeleton (Cheung and Wu 2008). The actin cytoskeleton facilitates the transport of biosynthetic materials to the growing tip, including cellulose synthase and callose synthase, both trafficked in Golgi-derived bodies (Cai et a.l 2010). Actin is also required for the integration of cargoes into the tip and for the recycling of membrane (Cheung and Wu 2008; Moscatelli et al. 2012). The study of spatiotemporal regulation of growth machinery in the growing pollen tube faces the challenges of observing any dynamic system: in order to fully understand a process it may be necessary to recognise and quantify large numbers of individual cellular components, quantifying their interaction with actin filaments in a highly dynamic manner. Much information is available from biological images of these dynamic systems, yet meaningful quantitative analysis is often difficult to be done accurately by hand and eye, especially when analysing the dynamic interactions of subpopulations of individual entities. Here, we take a computational approach to quantitatively analyse the association of mitochondria with actin filaments in growing pollen tubes. Rapid transport of mitochondria in pollen tubes has been shown to be dependent on the actin cytoskeleton (Zheng et al. 2010), and mitochondrial dynamics can be used as an indicator of the rate of actin-mediated cytoplasmic streaming and cargo transport. Mitochondrial movement can range from low speed, < 5 μm·s−1 movements to dashes along actin filaments at rates up to 10 μm·s−1 (Van Gestel et al. 2002; Zheng et al. 2009; Zheng et al. 2010). Motion is believed to be predominantly powered by myosin motor proteins, although a role for actin dynamics in mitochondrial movement has also been suggested (Sparkes et al. 2008; Avisar et al. 2009; Zheng et al. 2009) with myosin alone producing the low speed movements and a combination of actin dynamics and myosin action resulting in rapid dashes (Zheng et al. 2009). In addition, microtubule dynamics also have effects on mitochondrial velocity, trajectory and positioning in pollen tubes via their role in directing the arrangement of actin filaments (Zheng et al. 2010) or by providing tracks for low-speed movement and anchoring (Romagnoli et al. 2007).

Using the same object-based algorithms as for NET1A-GFP:plasmodesmata colocalisation we demonstrate a novel approach that can be used to effectively quantify dynamic interactions in a complex system, and quantitatively analyse the interactions of mitochondria (discrete objects) with actin filaments (a continuous object) in the growing pollen tube. This algorithm can, with user-defined adjustments, be used to study the colocalisation of static discrete objects and static continuous objects, as well as dynamic interactions between colocalising structures.

Materials and Methods

Plant Growth and Sample Preparation

Seedlings were grown on MS salts (Sigma, M5524) with 0.8% plant agar (Duchefa) under standard growth conditions (16 hours light, 22°C day temperature, 16°C night temperature). Stable transgenic *Arabidopsis thaliana* seedlings expressing the NET1A-GFP fusion protein, under the control of the native NET1A promoter, were incubated for 10 minutes in 0.1% aniline blue solution at pH 9.5 before imaging.

For dynamic studies using *Arabidopsis thaliana* pollen tubes, we used plants stably expressing the fluorescent actin reporter, RFP-FABD2, controlled by the pollen-specific Lat52 promoter. Pollen was germinated as described by Boavida and McCormick (2007), with incubation periods of 3-6 hours at 22°C. Prior to imaging, samples were incubated for 10 minutes with 2 µM MitoTracker Green® FM (Life Technologies) in liquid pollen germination media.

Imaging

Three-dimensional microscopy images of NET1A-GFP and aniline blue staining were acquired using an Andor Revolution XD spinning disk confocal microscope with an Andor iXon DU897E back-illuminated EMCCD with a pixel size of 0.220 µm by 0.220 µm. Z-stacks were collected with an Olympus PlanApoN 60x 1.42 NA oil lens at optimum z-spacing, according to the Nyquist–Shannon reconstruction theorem (Nyquist 1928; Shannon 1949), of 0.156 µm with each channel acquired sequentially at each step with laser/filter switching. NET1A-GFP was excited with a 488 nm laser and fluorescence collected via a band pass emission filter (510-540 nm) at 500 ms EMCCD exposure. Aniline blue was excited with a 405 nm laser and fluorescence collected via a band pass emission filter (417-477 nm) at 500 ms EMCCD exposure.

Four-dimensional time series of RFP-FABD2 and mitochondrial dynamics (MitoTracker green) were acquired again with the Andor Revolution XD spinning disk confocal microscope, pixel size 0.13 µm by 0.13 µm. Z-stacks were collected with an Olympus UPlanSApo 100x 1.4 NA oil lens at a z-spacing of 0.252 nm (10 slices, 2.52 µm). Stacks were repeated 48 times, once every 20 seconds. Channels were acquired sequentially. MitoTracker Green was excited with a 488 nm laser and RFP-FABD2 was excited with a 561 nm laser with fluorescence collected via a dual band pass emission filter (512 nm and 630 nm). Excitation lasers are alternated by rapid AOTF switching. Both images were collected at 32 ms EMCCD exposure with an average of 32 exposures.

Focusing different wavelengths through the same lens lead to slight differences in the focussed position; this shift is known as chromatic aberration. Chromatic aberration can be largely compensated by the use of apochromatic lenses, as used in this paper; however, non-lens based sources of chromatic aberration (e.g. differences between plane of coverslip and plane of slide, optical path misalignments, etc.) may also affect final images. We used carboxylate-modified polystyrene latex beads of 0.03 µm mean diameter (L5155, Sigma-Aldrich, St. Louis, MO, US) that have excitation and emission spectra most closely suited for the two-wavelength setup used in this paper. Beads were diluted to a concentration of 1:1000, sonicated, air-dried on a coverslip, embedded in Vectashield, sealed on a slide and imaged using

the same parameters as for the NET1A-GFP study. The images were then run through the same colocalisation program as the cellular images. For the field of view used, 75 beads were identified at both wavelengths. Vector shifts between a bead's centroid in the red channel and green channel were analysed and the average values in three dimensions used as a measure of translational shift. The average shift in each dimension was smaller than the uncertainty due to centroid bias (below), as such no chromatic aberration correction was applied to the final data.

Image Processing

Illumination Correction and Normalisation

In fluorescence microscopy, uneven background illumination, or vignetting, can cause serious problems when undergoing analysis: bright regions of background can obscure desired foreground signals, i.e. data. In order to decrease the obscuring of data by the background many different techniques can be applied to estimate the background illumination and thus remove the background signal, (e.g. Babaloukas et al. 2011).

For the 3D colocalisation of NET1A and plasmodesmata labelling we used a relatively simple background approximation technique: low-pass filtering. Low-pass filtering selects for low-frequency signals and attenuates high-frequency signals in the images. Very high-frequency signals in an image are often noise and this technique is used to 'smooth' an image, removing such noise. Using a low-pass filter with a very low cut-off removes not just noise but also foreground signals; what remains is a good approximation of the background illumination.

While it is possible to run such a filter on a 3D volume, due to the spinning disk imaging modality, the uneven illumination for these images was restricted to each 2D x-y plane. As such, we ran 2D background illumination correction on each frame using the algorithm in Fig. 1 (Algorithm 1). The value of σ used for each sequential Gaussian filter is an integer from 1 to a user-defined maximum, which should be selected dependent upon the size of foreground objects. The early filters, with a low value of σ, will remove small signals such as noise, whilst the later filters, with higher values of σ, will remove larger signals, i.e. foreground objects. For this data we used rotationally symmetric Gaussian low-pass filters with kernel size 3σ and standard deviation of $\sigma = 20$.

For colocalisation of MitoTracker and RFP-FABD2 labelling we did not use full-image background illumination correction techniques; instead it was necessary to create a mask of the pollen tube region. For the MitoTracker channel the minimum and maximum intensity values within the mask were used to normalise the image, giving the image a maximum dynamic range for the signal within the pollen tube (Fig. 1; Algorithm 2). This gives the signal within the pollen tube the maximum dynamic range possible, whilst preventing signals from outside the pollen tube from interfering with the colocalisation algorithm. Hot pixels, i.e. noise-related pixel with a high intensity value, were eliminated across the image series to ensure that the dynamic range after normalisation was biologically meaningful.

Object-Based Colocalisation

Object-based colocalisation in this paper is based on the algorithm proposed by Obara et al. (2013), which is based on 3D blob-like detection as described in Obara et al. (2008). This is a two stage detection algorithm: detection of all blob-like signals followed by matching and pruning. All steps are carried out in 3D.

The local blob detection algorithm (Fig. 1; Algorithm 4) uses an expected blob size, for NET1A-GFP and aniline blue signals this size was a 260 nm radius sphere, to identify likely candidates. The expected blob size is used in the Laplacian of Gaussian convolution of the image and the statistical pruning of blob candidates. Blob candidates are selected from local maxima in the image with intensity above a user-defined threshold; the user-defined threshold is selected to prevent noise being selected as blobs. All blobs are treated as ellipsoids for descriptor and centroid calculation before undergoing statistical pruning of candidates. Weighted centroids are then calculated before candidates in both images are paired using the Hungarian matching algorithm. As blobs are matched they are removed from the image to prevent mismatching.

For MitoTracker-actin colocalisation, MitoTracker signals were identified as above, with an expected blob radius of 0.75 µm. Actin cables were then segmented using a mean thresholding technique (Fig. 1; Algorithm 3); this technique identified all pixels from the actin channel images that are within actin cable signals. The ellipsoids calculated from the MitoTracker signals are then used to identify putative colocalising actin pixels (Fig. 2). The putative matches are then run through a Hungarian matching algorithm to identify all actin pixels that colocalise with mitochondrial signals.

Due to the nature of the centroid calculation algorithm used in our and many other programs, there is a centroid bias in the program. The centroid, which is refined with an intensity weighted centre of mass algorithm, is biased toward the centre of pixels for small signals, i.e. one or two pixels. Fig. 3 shows how sub-pixel signals emanating from the corners and sides of a pixel's region of view are drawn in towards the centre of the pixel. This adds an unknown uncertainty to all measurements of distance between two centroids. For the purpose of the below results we have assumed a minimum uncertainty of 0.5 pixels in each direction (i.e. 170 nm in 3D Euclidean distance); this the maximum uncertainty due to centroid bias between two points. For signals larger than one pixel, this centroid bias becomes negligible as the bias from each pixel helps to cancel bias of neighbouring pixels.

Pixel-Based Colocalisation

Colocalisation analysis as described in Deeks et al. 2012 was performed by selecting square regions of interest (150 by 150 pixels in x-y) within the dataset where punctae in both the red and green channels were of superior contrast. Background fluorescence was removed from the colocalisation analysis using masks generated by the 'threshold' tool of ImageJ. The threshold selected for each ROI depended upon the local level of background fluorescence as this level was not consistent throughout the dataset. Eight images encompassing 10 cells were combined onto one canvas in ImageJ and analysed using ColocalizerPro (Colocalization Research Software) to generate a Pearson's correlation value. The negative control value was obtained by displacing the red and green channel data by 11 pixels along the y axis. Regions of interest and masks were duplicated and displaced accordingly.

Software Packages

Object-based colocalisation algorithms were implemented off-line using the software package MATLAB and Image Processing Toolbox Release 2012b (The MathWorks, Inc., Natick, Massachusetts, USA). The full algorithm, as used in this paper, is available from the corresponding author.

Pixel-based colocalisation used ImageJ (National Institutes of Health, Bethesda, Maryland, USA) to generate masks and were analysed with CoLocalizer Pro (CoLocalization Research Software).

Results

Colocalisation of NET1A with Plasmodesmata

To demonstrate the performance of our technique we have re-analysed a dataset first published by Deeks et al. 2012. This z-stack of images of *Arabidopsis thaliana* root meristems was collected using spinning disk confocal microscopy. Nano-domains along plasma membranes were labelled using two probes. The first was a Green Fluorescent Protein (GFP) fusion to the actin binding protein NET1A (NET1A-GFP) a protein which localises to the plasma membrane and concentrates at plasmodesmata and suggested to be involved in the link between the actin cytoskeleton and the plasma membrane. NET1A-GFP localises to distinct punctae along the plasma membrane. The second probe was aniline blue, a dye excitable at 405 nm that labels callose-rich cell-to-cell junctions called plasmodesmata. The signal along the plasma membrane domains was isolated using a threshold approach and the correlation between pixel intensities was measured using the Pearson's coefficient (pixel-based colocalisation; Materials and Methods). This gave a positive value of 0.859 suggesting a strong coincidence between the NET1A-GFP structures and plasmodesmata. A maximum value of 1 denotes an absolute correlation of pixel intensities but should be impossible to obtain due to random noise and optical constraints.

In this particular case the Pearson's correlation value does not give a quantity that can be related to the distance distribution between the nano-punctae of the two channels. Variability throughout the image of fluorescence from out-of-focus planes, instrument noise and auto-fluorescence prevents the effective masking of background signal from the correlation calculation. To understand whether green (NET1A) nano-punctae perfectly coincide with red (plasmodesmata) it would be necessary to compare Pearson's correlation values between a number of control experiments to test alternative hypotheses. Ideally these would use two alternative fluorescent labels of equivalent intensity to aniline blue. The first label would localise homogeneously across the cell wall, while the second would highlight the zones between plasmodesmata. These ideal probes are not available. To estimate the element of background fluorescence the two channels were displaced by 11 pixels, giving a Pearson's correlation value of 0.132. Confidence that the difference of 0.727 represents colocalisation at the resolution of nano-domains is derived from high-resolution transmission electron microscopy imaging combined with an immunoaffinity label (Deeks et al. 2012). These techniques showed that NET1A protein specifically localises to within nanometers of the membrane surrounding plasmodesmata. Such tools and techniques are expensive, time consuming and rely upon specialist skills and equipment. More highly resolved optical solutions to image nano-structures are often limited by the brightness and specific

characteristics of the probes. There is a requirement for an alternative method to extract higher-quality quantitative colocalisation results from fluorescence imaging data.

The probe signals for each label were isolated using a local maxima detection approach and candidates were colocalised between channels using the Hungarian matching algorithm (Fig. 4). Of 954 NET1A-GFP signals identified, 682 colocalise with signals from aniline blue; there were a total of 1162 individual aniline blue signals. As a control we shifted the image three pixels horizontally, to keep plasma membrane with plasma membrane and cytoplasm with cytoplasm whilst shifting the nano-domains enough to alternate (rather than superimpose) red and green punctae. The resultant image showed that only 351 of 1162 NET1A signals now colocalise with aniline blue signals; there were a total of 954 aniline blue signals. The decreased number of detected NET1A signals is due to 'lost' pixels at the image boundary due to the shift.

The algorithm allows more than just looking at whether signals colocalise or not. Because of the object-based nature the program can also find the Euclidean distance of any colocalising signals, i.e. the distance between a NET1A-GFP and an aniline blue signal. (Fig. 5 (a,b)) shows this information in two formats; (a) shows a 3D representation of the colocalising pairs, colour coded based upon their distances whilst (b) shows a maximum z-projection with the data overlaid. Fig. 5 (c) shows distance histograms for the data (blue) and the control (red; see above). The mean colocalisation distance of the population is 330 nm. The distance at which 50% of objects colocalise (CD50) is approximately 250 nm. The mean value for the control is 685 nm with a CD50 of approximately 700 nm. It is clear from the superimposed histograms (Fig. 5 (c)) that a 660 nm spatial shift has resulted in an almost equal displacement of the colocalisation distances. To compare, we repeated the three-pixel control using the Pearson's coefficient workflow. The modest shift in red and green channels generated a correlation value of 0.66. Although this is reduced from the original value of 0.86 it still indicates a positive correlation despite the 660 nm shift. The object-based method allows intuitive quantification of colocalisation patterns whereas the Pearson's coefficient is difficult to interpret. Pixel-perfect co-alignment of the channels is required for maximum correlation, as would be expected from two components of plasmodesmata, but this correlation is not completely broken by the shift in channels.

Fig. 5 (d) shows the intensity difference between channels of colocalised pairs. For each pair, the absolute difference between normalised intensity of signal on each channel is plotted. The 3D data has been overlaid onto a maximum z-axis projection of the aniline blue channel, which shows that the difference increases where the aniline blue signal is brighter; this acts as a good control to show that bleed through of signal is not the cause of colocalisation. If bleed through were a major issue then one would expect the difference between channels to remain similar for all colocalising pairs or to vary only due to uneven illumination of the brighter channel.

It is also possible to extract a biological context from this control. Assuming that aniline blue stains proportionally to callose content, the intensity difference is a quantification of the ratio of NET1A accumulation against callose content. It can be seen from Fig. 5 (d) that at the local level NET1A-GFP and callose content are closely linked as the variation of intensity difference between neighbouring

plasmodesmata is much less when compared to variation between neighbouring cell files and distant regions.

NET1A-GFP signal within the dataset is not distributed evenly at the tissue-scale. The cell files at the root-cap epidermis are devoid of GFP signal. Neighbouring cell files show an asymmetric signal, due to differential expression of NET1A. The outcomes are two distinct zones of 'orphan' aniline blue punctae to the right and far left of the field of view. This could be compensated for by either masking the zones lacking NET1A-GFP signal or by discounting the ratio of paired-to-unpaired aniline blue punctae and measuring only the paired-to-unpaired NET1A-GFP ratio (since NET1A-GFP punctae always appear in zones with strong aniline blue signal). We have opted for the latter since the boundaries of any mask proved to be subjective.

Our results confirm the colocalisation of plasmodesmata (aniline blue) and NET1A (GFP) as originally reported in Deeks et al. (2012). Further, we have produced quantified results that show the distances between colocalising pairs and quantified results showing the direction of displacement and the intensity of signals which can be used in further experiments and to gain both imaging and biologically relevant information.

Colocalisation of Mitochondria with Actin Filaments across Time

To demonstrate the extent of our technique we produced a data set showing the association of mitochondria, labelled with MitoTracker, and actin filaments (RFP-FABD2); this shows how our algorithms can be used in a novel way: to examine the colocalisation of discrete objects with a continuous object. Further, this data was extended into four dimensions: a 3D time series. The time series of images of *Arabidopsis thaliana* pollen tube was collected using spinning disk confocal microscopy. The MitoTracker labelling of mitochondria shows these as distinct punctae throughout the pollen tube whilst the actin-binding RFP fusion protein labels filamentous actin within the pollen tube. Quantifying association of these two probes is a unique situation: usually colocalisation examines whether or not two sets of 'blobs' are associated, here we must look at whether one set of 'blobs' is associated with any sub-domain of a 'cable' or 'network'.

Fig. 6 shows an example segmentation of the actin network within the pollen tube and the associated mitochondrial signals. In areas of the pollen tube with indistinct actin signals (i.e. the pollen tube tip) there is little to no segmentation of actin cables or colocalisation of mitochondria with actin. This region of the pollen tube contains a more motile and unbundled network of filamentous actin required to integrate vesicles into the pollen tube tip.

Fig. 7 shows how bleaching of the image affects the segmentation of actin cables and thus the colocalisation program. Fig. 7 (a) shows that the overall identifiable volume of the pollen tube, as used in the masking process, did not change much with time; however, it should be noted that the length of the pollen tube increased during the imaging time but the segmentable actin cable network did not invade the new volume. However, it is clear from the raw data (not shown) that actin segmentation volume decreased with an apparent exponential drop with time. Fig. 7 (b) shows exponential curve fitting for the volume of actin segmented at each time point (red; $y = 0.94\exp[-0.012x]$) and the mean

pixel intensity within the pollen tube mask (blue; $y = 0.93\exp[-0.016x]$); both graphs have been normalised such that the maximum mean pixel intensity or maximum actin volume segmented equates to one.

The segmentation of actin by the program depends upon the amount of RFP-FABD2 signal above a certain threshold limit; if the intensity of the image decreases then either less filamentous actin will be detected or those cables detected will be 'seen' as thinner, i.e. have a lower segmented volume. Having observed these images manually we find that the code detects clear actin filaments in all time frames; however, the apparent width of actin filaments detected decreases with time (see Fig. 7 (d) for a diagrammatic explanation). This decrease in apparent width seems to match the decrease in brightness of the RFP-FABD2 signal within the pollen tube. Fig. 7 (c) shows how the average distance between segmented actin cables increases with time; this increase suggests that the program is identifying thinner cables within the image.

A further example of bleaching is in the first frame of this data (not shown). The data in this frame was very hard to extract and still results in quantified data noticeably different from the subsequent frames. It is plausible that the pre-imaging accumulation of fluorescent molecules within mitochondria and non-specific labelling is responsible for this difference. Continuous replenishment of mitochondrial fluorescence due to oxidation of mitochondrial MitoTracker may make these objects more resistant to bleaching effects than non-specifically labelled artefacts. Many of the applied correction techniques, e.g. masking and normalisation, helped to increase the number of segmentable MitoTracker signals and help give a better colocalisation result when compared manually to the data.

Fig. 8 shows the number of MitoTracker signals (mitochondria) and the number of colocalising mitochondria for each time-point of the series. The number of identified mitochondria signals increases slightly with time whilst the number of signals 'colocalising' with actin decreases with time. The increase in mitochondria signals is due to an overall increase of mitochondria across the pollen tube (data not shown) rather than in a particular region of the tube. Unfortunately, the decrease in number of colocalising mitochondria signals appears to be due to the bleaching artefacts of the actin channel and follows a mild exponential decrease. The numbers of mitochondria in the pollen tube tip region, where actin cables are diffraction-limited and do not segment clearly, did not increase dramatically (data not shown); further human viewing of the time-series shows that the decrease in colocalising mitochondria is apparently evenly distributed across the rest of the tube.

Our results show that the quantification of organelles as they are transported along cytoskeletal systems is a highly achievable goal. Our data also shows that bleaching through time is a major factor influencing the results from such an experiment. The data above has been shown to demonstrate both of these sides of bioimage informatics: novel techniques allowing access to new measurements and quantifications and possible pitfalls in striving for these new tools.

Discussion

Extracting Sub-Resolution Information of NET1A

We have used algorithms to automatically detect individual plasmodesmata within the crowded three-dimensional environment of the *Arabidopsis thaliana* root apex. Co-imaging of two markers for plasmodesmata (aniline blue for cell wall callose and NET1A-GFP for plasmodesmal membrane) has allowed us to demonstrate the utility of this technique in quantifying three-dimensional colocalisation relationships within populations. 71% of plasmodesmata labelled with aniline blue can be matched with foci of NET1A-GFP. Approximately 75% of these partners have weighted centroids that lay less than 400 nm apart. Artificially displacing the two channels by just 3 pixels shows obvious disruption of this colocalisation pattern in line with expectations. By contrast the alternative method of assessing colocalisation using Pearson's correlation testing provides no spatial quantities. Fig. 9 describes the potential ultrastructure of the observed plasmodesmata based on TEM data (Deeks et al. 2012). Individual pores will differ in their orientations but the pore presented in Fig. 9 is drawn to show the organisation of components in channels along apical-basal cell walls (horizontal cell walls as viewed within Fig. 4 and Fig 5). The cell wall interrupts the callose sphincters at either end of the pore. In theory it should be possible with sufficient magnification and numerical aperture to differentiate between symmetrical and asymmetrical deposition of components across the pore (Fig. 9 (b)). Our dataset however was not optimised for high-resolution analysis. Ideally we would require data at the Nyquist resolution (approximately three times the magnification of the current data set). Such a resolution would decrease the uncertainty associated with the centroid bias, along with implementation of possible bias reducing techniques, and allow information to be gleaned at a resolution below that of the cell wall thickness.

Along with this higher resolution comes further information that can be extracted from object-based colocalisation techniques. We were also able to produce maps, such as those in Fig. 5, which show the direction between colocalising pairs (not shown). With greater resolution we could identify if there was any consistent direction of displacement between colocalising signals, i.e. any asymmetry within the system.

Further, the use of an intensity difference map (Fig. 5 (d)) may lead to a novel quantifiable feature that can be used to discriminate between different plasmodesmal fluorescent markers. It would be of great interest to compare maps of various live-cell plasmodesmal markers as it might be possible, using this program and the intensity difference maps, to discriminate between markers that localise proportionally to the number of channels and markers that specifically respond to the local callose content of the cell wall. This could potentially differentiate between. ‘open’ vs. ‘closed’ plasmodesmata in living tissue responding to stimuli in real time.

Co-imaging of Motile Mitochondria and Cytoskeletal Tracks

Co-imaging and population analysis of mitochondria and actin filaments within the pollen tube has shown that not all mitochondria colocalised with actin cables. This is perhaps not surprising as the association of mitochondria with microtubules has been documented as transient in the pollen tube (Romagnoli et al. 2007). Romagnoli and colleagues (2007) proposed a model of antagonistic action of microtubules and actin filaments on the movement of mitochondria at the pollen tube cell cortex. Cortical microtubules provide a means of anchoring mitochondria during their motion towards the

pollen tube tip. Observation of the movement of purified pollen tube mitochondria shows that their movements on actin are salutatory rather than processive. Also, removing microtubules *in vivo* using drug treatments helps to smooth the flow of mitochondria (Romagnoli et al. 2007). This opposes the situation in root hairs where the depolymerisation of microtubules increases the frequency of interrupted motion (Zheng et al. 2009). It would be interesting to repeat this experiment using our own dual-fluorescent pollen lines to test the hypothesis that the association of mitochondria with the actin cytoskeleton increase upon such treatments. Ideally, triple labelling to include the microtubule cytoskeleton would allow testing of the hypothesis that the organelles must be engaged with at least one cytoskeletal system at any one time. One limitation of the current experimental setup is that the fine cortical cables used for mitochondrial movement are difficult to image with the RFP-FABD2 probe. Longer exposure times are ideally required which would be incompatible with mitochondria movement. An extra fluorescent probe would compound this problem.

Prospective Pitfalls in Plant Bioimage Informatics

Showing the object-based colocalisation of mitochondria and actin filaments with time shows both the power of such a bioimage informatics tool and also how careful one must be to avoid major pitfalls. Bleaching can cause severe effects on the results of any computational analysis and easy to identify controls should be put in place to check that this is not the case. Fig. 8 shows how the distance between a colocalising MitoTracker signal and its matched actin signal is constant through the time series but how the percentage of MitoTracker signals considered colocalising decreases; this shows that the code is segmenting a decreased thickness of actin cables and is not currently able to compensate for this.

Actin filaments have a saturation limit for fluorescent binding proteins, these probe molecules exchange with a finite cytoplasmic pool and several seconds are required for bleach recovery of filament fluorescence. Due to the significant laser power used during imaging we feel that this decrease in segmented actin volume represents the increased proportion of bleached fluorophore within the pollen tube. We are currently comparing and developing techniques to correct for this bleaching either at the imaging or bioimage informatics stages.

One possible compensation is to consider that all actin cables are likely to be sub-resolution in this particular microscopy set-up; therefore, one solution is to segment the actin cables and set the diameter of all cables to 200 nm. Another option would be to adapt the threshold for actin segmentation based on an a priori bleaching curve or, indeed, by matching a curve to some measure of bleaching, e.g. actin volume, for the data set and post-processing before re-computing the actin segmentation.

A technique that has applications for many bioimage informatics problems is to consider the actin probe signal as a representation of a skeletal network, i.e. a network of one voxel thickness at any point. The branches of these networks would be single voxel thick skeletal lines in 3D space; this would remove issues relating to the thickness of actin cables but requires high enough resolution to make out individual actin filaments.

Many articles on ideal bioimage informatics or image processing and analysis emphasise the issue of assumptions: without clearly stating assumptions when designing and publishing algorithms and

programs for automated analysis of images, errors can begin to build in application and evaluation of the program and its data. There is, however, a problem of accidental assumptions: algorithmic bias. We have described how intensity-based object centroid calculation has an inherent bias, a problem we hope to address in future versions of this code. Other such biases often occur in programs designed for automated analysis and, unless made fully open to program users, such biases could cause misinterpretation of results, e.g. the dip in the second bin of Fig. 5 (c), without realising the cause of such results. This particular bias becomes negligible for object much greater than one voxel in size, hence further magnification to Nyquist limits is important in the initial imaging stages.

The object-based colocalisation techniques that have been showcased in this paper show not only the power of relatively simple bioimage informatics tools but the ability of well-designed tools to be applied to multiple imaging scenarios. As new scenarios are approached the bioimage informatists working with a code can improve and adapt the code, giving it more abilities or making it more accurate; these adaptations can be saved in a modular-like manner, allowing a single code to be adapted for multiple situations based upon the needs of the biologist, the imaging modality, issues with the images and the question being asked. With this in mind, the program used in this paper is currently being refined and adapted further; it is hoped that issues like bleaching, hot pixels or poor dynamic range can be fixed using computational and statistical methods that can be turned on and off by the user. The final program will hopefully be released as part of a larger project currently ongoing.

Future work

This article has showcased object-based colocalisation in plant sciences; we have highlighted the power of such techniques and also the pitfalls that researchers can fall into. We also intend to continue development by including the tracking of trafficked particles, e.g. mitochondria, along networks, such as actin filaments, within time series. Expansion of the program in this way would allow biologists to study if/how/when mitochondria, or any other labelled particles, are trafficked to particular places, such as the growing pollen tube tip. With continuing rapid improvements in microscopes and microscopy techniques it may be possible to view this trafficking with fantastic resolution in not just the x-y plane but in the orthogonal and temporal planes, creating a mass of available ‘phenotypic’ data that can be used to probe existing models or to identify the functions of novel genes.

One area of bioimage informatics research that we are currently pursuing is the improvement of techniques for segmentation of networks, such as actin, from standard resolution imaging techniques. With optimally segmented actin networks and strong compensation for bleaching effects, it will be possible to use dynamic object-based colocalisation techniques to study much more than just how many colocalise and when but to study questions such as ‘are trafficked mitochondria colocalised with actin for their entire journey?’ or ‘is trafficking different at newly formed actin networks, e.g. the pollen tube tip, compared to established cables, i.e. far from the tip?’. This aim is part of a larger project that is currently ongoing and we hope to release in the form of a GUI-fronted program or plug-in for use by other researchers.

Acknowledgments

NET1A dataset used for method validation previously generated as part of projects supported by the Biotechnology and Biological Sciences Research Council (BB/G006334/1). The bioimage informatics work in this paper was supported by an academic grant from the The Royal Society, UK (RF080232).

With warm thanks to Martin R. Dixon, Durham University, for Lat52-RFP-FABD2 *Arabidopsis thaliana* lines as used in mitochondrial tracking along actin filaments.

References

Allan, C., Burel, J.-M., Moore, J., Blackburn, C., Linkert, M., Loynton, S., MacDonald, D., Moore, W. J., Neves, C., Patterson, A., Porter, M., Tarkowska, A., Loranger, B., Avondo, J., Lagerstedt, I., Linias, L., Leo, S., Hands, K., Hay, R. T., Patwardhan, A., Best, C., Kleywegt, G. J., Zanetti, G. and Swedlow, J. R. (2012). OMERO: flexible, model-driven data management for experimental biology. *Nature Methods*, **9**(3), 245–53.

Avisar, D., Abu-Abied, M., Belausov, E., Sadot, E. and Hawes, Sparkes. (2009). A comparative study of the involvement of 17 Arabidopsis myosin family members on the motility of Golgi and other organelles. *Plant Physiology*, **150**, 700–709.

Babaloukas, G., Tentolouris, N., Liatis, S., Sklavounou, A. and Perrea, D. (2011). Evaluation of Three Methods for Retrospective Correction of Vignetting on Medical Microscopy Images Utilising Two Open Source Software Tools. *Journal of Microscopy*, **244**(3), 320-324.

Boavida, L. C., McCormick, S. (2007). Temperature as a Determinant Factor for Increased and Reproducible *In Vitro* Pollen Germination in *Arabidopsis thaliana*. *The Plant Journal*, **52**(3), 570-582.

Cai, G., Faleri, C., Del Casino, C., Emons, A., and Cresti, M. (2011). Distribution of Callose Synthase, Cellulose Synthase, and Sucrose Synthase in Tobacco Pollen Tube Is Controlled in Dissimilar Ways by Actin Filaments and Microtubules. *Plant Physiology*, **155**(3), 1169–1190.

Cardona, A., and Tomancak, P. (2012). Current challenges in open-source bioimage informatics. *Nature Methods*, **9**(7), 661–5.

Carpenter, A. E., Kamentsky, L., and Eliceiri, K. W. (2012). A call for bioimaging software usability. *Nature Methods*, **9**(7), 666–670.

Cheung, A. Y., & Wu, H. (2008). Structural and signaling networks for the polar cell growth machinery in pollen tubes. *Annual Reviews*.

Cho, B. H., Cao-Berg, I., Bakal, J. A., and Murphy, R. F. (2012). OMERO.searcher: content-based image search for microscope images. *Nature Methods*, **9**(7), 633–4.

Cobb, J. N., Declerck, G., Greenberg, A., Clark, R., and McCouch, S. (2013). Next-generation phenotyping: requirements and strategies for enhancing our understanding of genotype-phenotype relationships and its relevance to crop improvement. *Theoretical and applied genetics,* **126**(4), 867–87.

Deeks, M. J., Calcutt, J. R., Ingle, E. K. S., Hawkins, T. J., Chapman, S., Richardson, A. C., Mentlak, D. A., Dixon, M.R., Cartwright, F., Smertenko, A.P., Oparka, K. and Hussey, P. J. (2012). A Superfamily of Actin-Binding Proteins at the Actin-Membrane Nexus of Higher Plants. *Current Biology*, **22**(17), 1595-600.

Dhondt, S., Van Haerenborgh, D., Van Cauwenbergh, C., Merks, R. M. H. H., Philips, W., Beemster, G. T. S. S., and Inzé, D. (2012). Quantitative analysis of venation patterns of Arabidopsis leaves by supervised image analysis. *The Plant Journal: for Cell and Molecular Biology*, **69**(3), 553–563.

Eliceiri, K. W., Berthold, M. R., Goldberg, I. G., Ibáñez, L., Manjunath, B. S., Martone, M. E., Murphy, R. F., Peng, H., Plant, A. L., Roysam, B., Stuurman, N., Swedlow, J. R., Tomancak, P. and Carpenter, A. E. (2012). Biological imaging software tools. *Nature Methods*, **9**(7), 697–710.

Fichtl, A., Sailer, M., Brenner, R. E., Schmidt, V., Walther, P., Lück, S., and Joos, H. (2011). Statistical analysis of the intermediate filament network in cells of mesenchymal lineage by greyvalue-oriented image segmentation. *Computational Statistics*, **28**(1), 139–160.

Gelasca, E. D., Obara, B., Fedorov, D., Kvilekval, K., Manjunath, B. S. (2009). A Biosegmentation Benchmark for Evaluation of Bioimage Analysis Methods. *BMC Bioinformatics*, **10**, 368-79.

Goff, S. A, Vaughn, M., McKay, S., Lyons, E., Stapleton, A. E., Gessler, D., Matasci, N., Wang, L., Hanlon, M., Lenards, A., Muir, A., Merchant, N., Lowry, S., Mock, S., Helmke, M., Kubach, A., Narro, M., Hopkins, N., Micklos, D., Hilgert, U., Gonzales, M., Jordan, C., Skidmore, E., Dooley, R., Cazes, J., McLay, R., Lu, Z., Pasternak, S., Koesterke, L., Piel, W. H., Grene, R., Noutsos, C., Gendler, K., Feng, X., Tang, C., Lent, M., Kim, S.-J., Kvilekval, K., Manjunath, B. S., Tannen, V., Stamatakis, A., Sanderson, M., Welch, S. M., Cranston, K. A., Soltis, P., Soltis, D., O'Meara, B., Ane, C., Brutnell, T., Kleibenstein, D. J., White, J. W., Leebens-Mack, J., Donoghue, M. J., Spalding, E. P., Vision, T. J., Myers, C. R., Lowenthal, D., Enquist, B. J., Boyle, B., Akoglu, A., Andrews, G., Ram, S., Ware, D., Stein, L. and Stanzione, D. (2011). The iPlant Collaborative: Cyberinfrastructure for Plant Biology. *Frontiers in Plant Science*, **2**(July), 34.

Hepler, P. K., Vidali, L., & Cheung, A. Y. (2001). Polarized cell growth in higher plants. *Annual Review of Cell and Developmental Biology*, **17**, 159–187.

Kleine-Vehn, J., Wabnik, K., Martinière, A., Łangowski, Ł., Willig, K., Naramoto, S. and Friml, J. (2011). Recycling, clustering, and endocytosis jointly maintain PIN auxin carrier polarity at the plasma membrane. *Molecular Systems Biology*, **7**, 540.

Kuhn, W. H. (1955). The Hungarian Method for the Assignment Problem. *Naval Research Logistics Quarterly,* **2**, 83–97.

Kvilekval, K., Fedorov, D., Obara, B., Singh, A., Manjunath, B.S. (2010). Bisque: a Platform for Bioimage Analysis and Management. *Bioinformatics*, **26**(4), 544-552.

Lichius, A., Goryachev, A. B., Fricker, M. D., Obara, B., Castro-Longoria, E. and Read, N. D. (2014). Functional Divergence of RAC1 and CDC42 Small GTPases During Cell Fusion in Neurospora crassa. *Journal of Cell Science*, In Press.

Ljosa, V., Sokolnicki, K. L., and Carpenter, A. E. (2013). Annotated high-throughput microscopy image sets for validation, *Nature Methods*, **9**(7), 1179–1180.

Lobet, G., Draye, X., and Périlleux, C. (2013). An online database for plant image analysis software tools. *Plant Methods*, **9**(1), 38.

Moscatelli, A., Idilli, A. L., Rodighiero, S. and Caccianiga, M. (2012). Inhibition of actin polymerisation by low concentration Latrunculin B affects endocytosis and alters exocytosis in shank and tip of tobacco pollen tubes. *Plant Biology*, **14**, 770–782.

Nyquist, H. (1928). Certain Topics in Telegraph Transmission Theory. *Transactions of the American Institute of Electrical Engineers,* **47**(2) .617-644.

Obata, B., Byun, J., Fedorov, D. and Manjunath, B. S. (2008). Automatic Nuclei Detection and Dataflow in BISQUIK System. *Workshop on Bioimage Informatics: Biological Imaging, Computer Vision and Data Mining*, Santa Barbara.

Obara, B., Grau, V., and Fricker, M. D. (2012). A bioimage informatics approach to automatically extract complex fungal networks. *Bioinformatics*, **28**(18), 2374–81.

Obara, B., Jabeen, A., Fernandez, N. and Laissue, P. P. (2013). A Novel Method for Quantified, Superresolved, Three-Dimensional Colocalisation of Isotropic, Fluorescent Particles. *Histochemistry and Cell Biology*, **139**(3), 391-402.

Peng, H., Bateman, A., Valencia, A., and Wren, J. D. (2012). Bioimage informatics: a new category in Bioinformatics. *Bioinformatics*, **28**(8), 1057.

Pound, M. P., French, A. P., Wells, D. M., Bennett, M. J., and Pridmore, T. P. (2012). CellSeT: novel software to extract and analyze structured networks of plant cells from confocal images. *The Plant Cell*, **24**(4), 1353–61.

Pridmore, T. P., French, A. P., and Pound, M. P. (2012). What lies beneath: underlying assumptions in bioimage analysis. *Trends in Plant Science*, **17**(12), 688–92.

Rajaram, S., Pavie, B., Hac, N. E. F., Altschuler, S. J., and Wu, L. F. (2012). SimuCell : a flexible framework for creating synthetic microscopy images. *Nature Methods*, **9**(7), 634–635.

Roeder, A. H. K., Chickarmane, V., Cunha, A., Obara, B., Munjunath, B. S., Meyerowitz, E. M. (2010). Variability in the Control of Cell Division Underlies Sepal Epidermal Patterning in A*rabidopsis thaliana*. *PLoS Biol* **8**(5): e1000367.

Rolland-Lagan, A.-G., Amin, M., and Pakulska, M. (2009). Quantifying leaf venation patterns: two-dimensional maps. *The Plant Journal: for Cell and Molecular Biology*, **57**(1), 195–205.

Romagnoli, S., Cai, G., Faleri, C., Yokota, E., Shimmen, T., and Cresti, M. (2007). Microtubule- and actin filament-dependent motors are distributed on pollen tube mitochondria and contribute differently to their movement. *Plant and Cell Physiology*, **48**(2), 345–61.

Sappl, P.G., and Heisler, M.G. (2013). Live-imaging of plant development: latest approaches. *Current Opinion in Plant Biology*, **16**(1), 33-40.

Shannon, C.E. (1949). Communication in the Presence of Noise. *Proceedings of the IRE* , **37**(1), 10-21.

Simpson, C., Thomas, C., Findlay, K., Bayer, E., and Maule, A. J. (2009). An Arabidopsis GPI-anchor plasmodesmal neck protein with callose binding activity and potential to regulate cell-to-cell trafficking. *The Plant Cell*, **21**(2), 581–594.

Sparkes, I.A., Teanby, N.A. and Hawes, C. (2008) Truncated myosin XI tail fusions inhibit peroxisome, Golgi, and mitochondrial movement in tobacco leaf epidermal cells: a genetic tool for the next generation. *Journal of Experimental Botany.* **59**, 2499–2512.

Swedlow, J. R., Goldberg, I., Brauner, E. and Sorger, P. k. (2003). Informatics and Quantitative Analysis in Bioimage Informatics. *Science*, **300**, 100-102.

Thomasson, M. S., and Macnaughtan, M. a. (2013). Microscopy basics and the study of actin-actin-binding protein interactions. *Analytical Biochemistry*, **43**(2), 156–165.

Van Gestel, K., Kohler, R.H. and Verbelen, J.P. (2002) Plant mitochondria move on F-actin, but their positioning in the cortical cytoplasm depends on both F-actin and microtubules. *Journal of Experimental Botany,* **53**, 659–667.

Yang, Y., Li, Y., and Wu, C. (2013). Genomic resources for functional analyses of the rice genome. *Current Opinion in Plant Biology*, **16**(2), 157–63.

Zheng, M., Beck, M., Muller, J., Chen, T., Wang, X., Wang, F., Wang, Q., Wang, Y., Baluska, F., Logan, D.C. et al. (2009) Actin turnover is required for myosin-dependent mitochondrial movements in Arabidopsis root hairs. *PLoS One,* **4**, e5961.

Zheng, M., Wang, Q., Teng, Y., Wang, X., Wang, F., Chen, T., Samaj, J. and Logan, D. C. (2010) The speed of mitochondrial movement is regulated by the cytoskeleton and myosin in *Picea wilsonii* pollen tubes. *Planta*, **231**(4), 779–91.

Algorithm 1: Background Illumination Correction

Input : I, σ
Output: I_c

1 **for** $z \in [1, \mathit{Depth}(I)]$ **do**
  /* for each z-slice in the image */
2 $imf \leftarrow I(z)$
3 **for** $s \in [1, \sigma]$ **do**
    /* for sequential kernel sizes */
4 $G \leftarrow \texttt{Gaussian}(s)$
5 $imf \leftarrow imf \star G$
    /* convolution with G */
6 **end**
7 $B(z) \leftarrow imf$
8 **end**
9 $I_c \leftarrow I - B$

Algorithm 2: Mask-based Normalisation

Input : $I, mask$
Output: I

1 $max \leftarrow \texttt{Maximum}(\texttt{Intensity}(I(mask)))$
2 $min \leftarrow \texttt{Minimum}(\texttt{Intensity}(I(mask)))$
3 **for** $\forall p \in I$ **do**
4 **if** $\mathit{Intensity}(p) < min$ **then**
5 $p \leftarrow min$
6 **else if** $\mathit{Intensity}(p) > max$ **then**
7 $p \leftarrow max$
8 **end**
9 $I \leftarrow \{i \in I : (\texttt{Intensity}(i) < min) \times min\}$
10 $I \leftarrow \{i \in I : (\texttt{Intensity}(i) > max) \times max\}$
11 $I \leftarrow (I - min)/(max - min)$

Algorithm 3: Segmentation of Cables

Input : I, r_x, r_y, r_z, s
Output: $Cables$

1 $S \leftarrow [s/r_x, s/r_y, s/r_z]$
2 $E \leftarrow \texttt{Ellipsoid}(S)$
3 $h \leftarrow I \star E$
4 $mean \leftarrow h/\texttt{sum}(h)$
5 $Cables \leftarrow I > mean$
6 $Cables \leftarrow \texttt{Reconstruct}(Cables, \texttt{Open}(Cables))$

Algorithm 4: Colocalisation of Blobs

Input : $I_1, I_2, r_x, r_y, r_z, s, T_1, T_2$
Output: $CoLoc$

1 $S \leftarrow [s/r_x, s/r_y, s/r_z]$
2 $L \leftarrow \texttt{LoG}(S)$
3 **for** $i \in [1, 2]$ **do**
  /* for each 3D channel */
4 $I_i \leftarrow I_i \star L$
5 $Candidates_i \leftarrow \texttt{LocalMaxima}(I_i)$
6 **for** $C \in Candidates_i$ **do**
    /* for each candidate */
7 $S_C \leftarrow \texttt{MeanIntensity}(\texttt{Shell}(C))$
8 $E_C \leftarrow \texttt{MeanIntensity}(\texttt{Ellipsoid}(C))$
9 **end**
10 $Blobs_i \leftarrow \{C \in Candidates_i : S_C < E_C)\}$
11 $Blobs_i \leftarrow \{B \in Blobs_i : \texttt{Intensity}(B) < T_i\}$
12 **for** $B \in Blobs_i$ **do**
    /* for each blob */
13 $E_B \leftarrow \texttt{Ellipsoid}(B)$
14 $D_B \leftarrow \texttt{Descriptor}(E_B)$
15 **end**
16 $Blobs_i \leftarrow \{B \in Blobs_i : \texttt{Prune}(B, D_B) = \text{FALSE}\}$
17 $W_i \leftarrow \texttt{WeightedCentroid}(\texttt{Ellipsoid}(Blobs_i))$
18 **end**
19 $CoLoc \leftarrow \texttt{HungarianMatching}(W1, W2)$

Fig.1 . Algorithm 1: Algorithm used for uneven background illumination correction of images. For this image series, correction was run on each 2D frame in turn. The algorithm takes a 3D image, *I*, and a sigma value. For each sequential filtering, a Gaussian low-pass filter of size 3*s* and standard deviation *s* is created, the filter is applied to the image through a convolution (the star symbol) operation, *s* is increased by one and the process is repeated until *s* equals *σ*. Once all sequential filtering steps have taken place, the over-smoothed image is the background approximation; this is removed from the original image. The output is a background corrected 3D image, I_c. Note: the ← symbol denotes 'becomes', e.g. line 2, *imf* becomes that z-slice of *I*; the ∈ symbol denotes 'an element of', e.g. line 3, for each element, *s*, of the interval [1,*σ*], i.e. all integers between 1 and *σ*. Algorithm 2: Algorithm used for pollen tube masking and normalisation of the dynamic range of MitoTracker within the mask.The algorithm takes the image, *I*, and a pollen tube mask, mask, and calculates the maximum, max, and minimum, min, intensity values within the mask. Any pixels in the image with intensity below the minimum are set to the minimum and likewise for pixels above the maximum. The whole image is then

normalised based on the pollen tube maximum and minimum intensity. Algorithm 3: Algorithm used for mean-based thresholding of actin cables. For a 3D image, an ellipsoid size *S*, scaled by the image resolution (R_x, R_y, R_z), is used as a kernel. The mean of the surrounding neighbourhood, as defined by the kernel, is calculated for each pixel .The value for each pixel is then compared to this mean; those pixels greater than the mean of their neighbourhood are counted as actin pixels. The thresholded image is then reconstructed by morphological opening. Morphological opening is the erosion followed by dilation of a binary image; reconstruction by morphological opening is a process by which the shapes of the actin cables can be more accurately extracted. Algorithm 4: Algorithm used for local-based colocalisation. Each step is carried out in 3D and each pre-processed and normalised channel (I_1, I_2) is analysed separately until centroids are matched in the final process. The Laplacian of Gaussian (LoG) convolution (star symbol) of each image enhances blob-like structures; after convolution the images are re-normalised. The filter size for the LoG convolution is determined by the resolution of the image in each direction (r_x, r_y, r_z) and the expected size of the blob, *s*. Local maxima are detected in each channel through morphological opening, identifying the locations of particles brighter than their immediate surroundings. Each candidate is given a centroid position and the ellipsoid around the candidate is calculated, a thin shell around this ellipsoid is also calculated. The comparison of the mean image intensity in the ellipsoid to the mean image intensity in the shell allows candidates to be checked and selected for. Those blobs with intensity above the user-set threshold, T_i for each channel, are then selected for. For this experiment, identified blobs are pruned using statistical measures. The remaining blobs are then given a weighted centroid and the blobs from both images are matched using the Hungarian matching algorithm (Kuhn 1955).

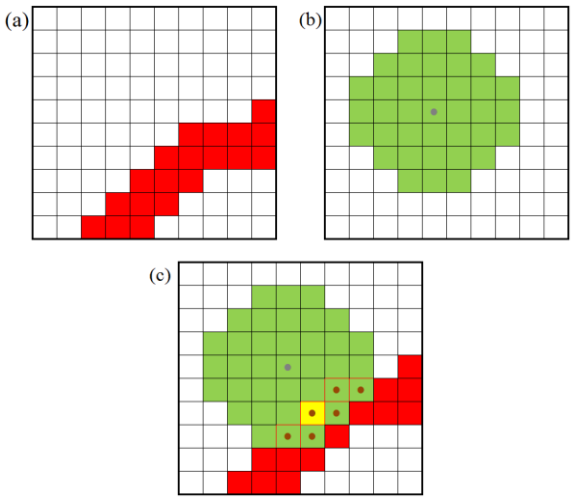

Fig. 2. A schematic explanation of actin-mitochondria colocalisation. (a) A pixel-by-pixel example of actin segmentation. Each square on the grid counts as a single pixel and each red square is a pixel that has been segmented as actin. (b) A mitochondrial 'blob' in green. The blob is centred on the mitochondrial centroid, labelled with a grey dot, as detected by the above algorithm. (c) Each actin pixel within the mitochondrial ellipsoid is considered a candidate for colocalisation; candidates are labelled with an orange dot. Of these candidates, only one is considered as a colocalising match, labelled yellow. This figure is a considerable simplification as many actin pixels may be candidates for matching to multiple mitochondrial signals. The technique used by this algorithm is designed to optimise the matching results.

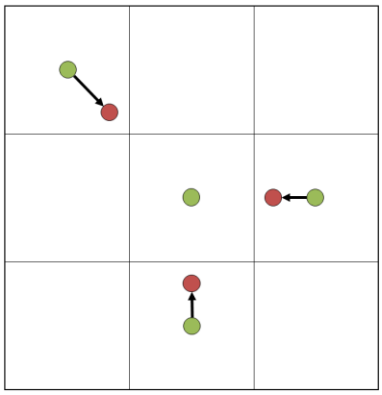

Fig. 3. Centroid bias of intensity-weighted centre of mass calculations draw the calculated position of objects towards the centre of pixels. A point of known position was placed in one of nine virtual sub-pixel regions; the figure shows a single pixel divided into those nine uniform regions. Each point was convoluted with a disc of diameter one pixel. This was repeated for all nine regions. Each artificial image then underwent centroid detection & weighted centroid refinement, as per the main algorithms. The figure shows the true centroid in green and an approximation of the calculated centroid in red, the arrows show the displacement of centroids towards the pixel centre. The signal centred on the pixel centre had negligible displacement (<0.01 of a pixel).

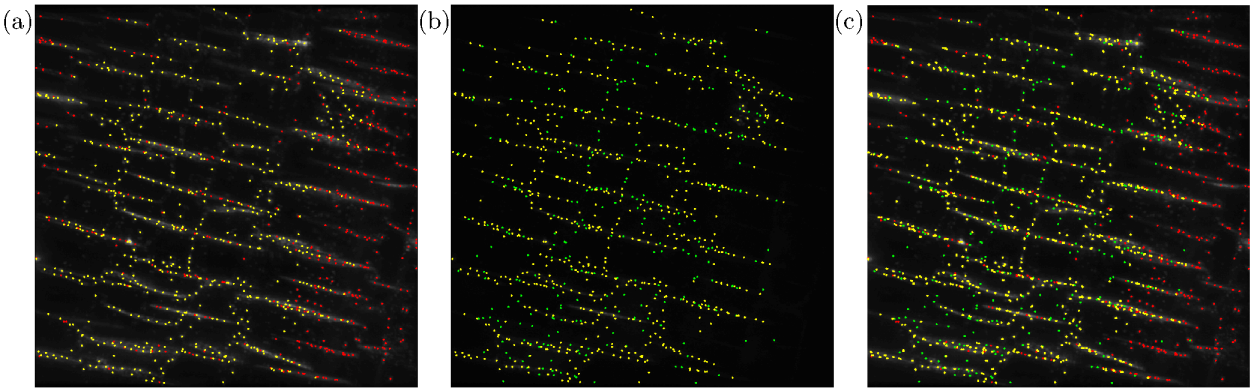

Fig. 4. NET1A-GFP colocalises with plasmodesmal signals as labelled with aniline blue. (a) Identified plasmodesmal labelling (aniline blue). Yellow dots (n=682) represent object-based colocalisation of plasmodesmal signals with NET1A signals; red dots (n=480) represent plasmodesmal signals that are not colocalised. (b) Identified NET1A-GFP signals. Yellow dots (n=682) represent object-based colocalisation of NET1A-GFP signals with plasmodesmal signals; red dots (n=272) represent NET1A-GFP signals that are not colocalised. (c) Merged channels show colocalisation of NET1A-GFP signals at plasmodesmal cell junctions as labelled with aniline blue. All images show a maximum projection through the z-axis.

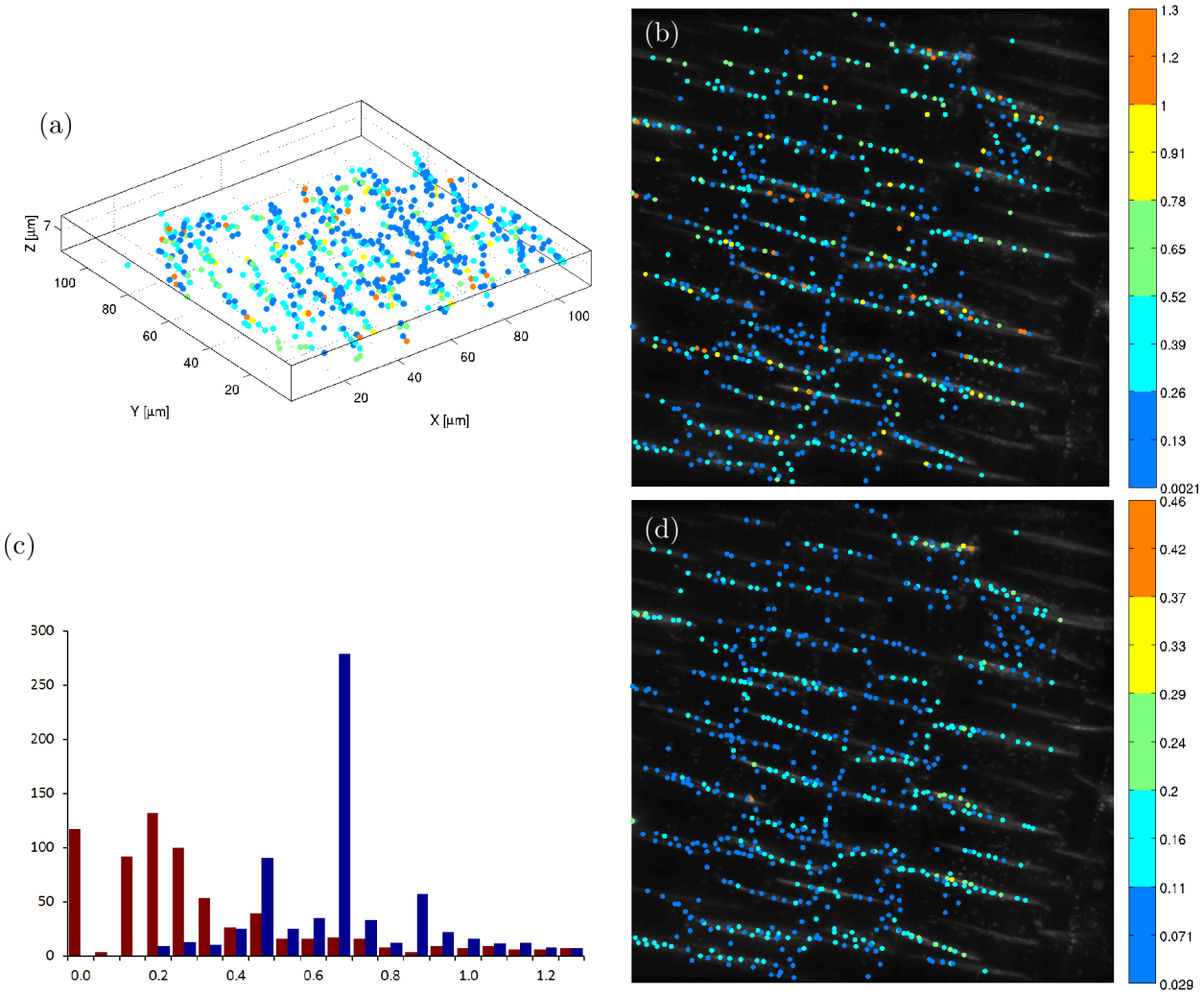

Fig. 5. (a) Euclidean distance map of colocalised object-pairs of NET1A-GFP and plasmodesmal cell junctions labelled with aniline blue. The scale runs from 0-260 nm (mid-blue) to 1-1.3 µm (orange), as indicated by the bar on the right of the figure. Note that this Euclidean distance carries a known uncertainty of ±170 nm due to centroid bias (above). The histogram of Euclidean distance to number of colocalisations is in the lower left of the scatterplot. (b) Distance map overlay with a maximum z-axis projection of the cells. (c) Distance histogram for colocalisation of NET1A-GFP and aniline blue signals. The blue histogram shows the distance distribution for the standard image (20 bins); note the drop in the second (0.07-0.13 µm) bin. The red histogram shows the distribution for the control image (see main text). (d) Intensity difference map of colocalised object-pairs of NET1A-GFP and plasmodesmal cell junctions labelled with aniline blue. The scale runs from 0.0-0.11 (mid-blue) to 0.37-0.46 (orange), as indicated by the bar on the right of the figure.

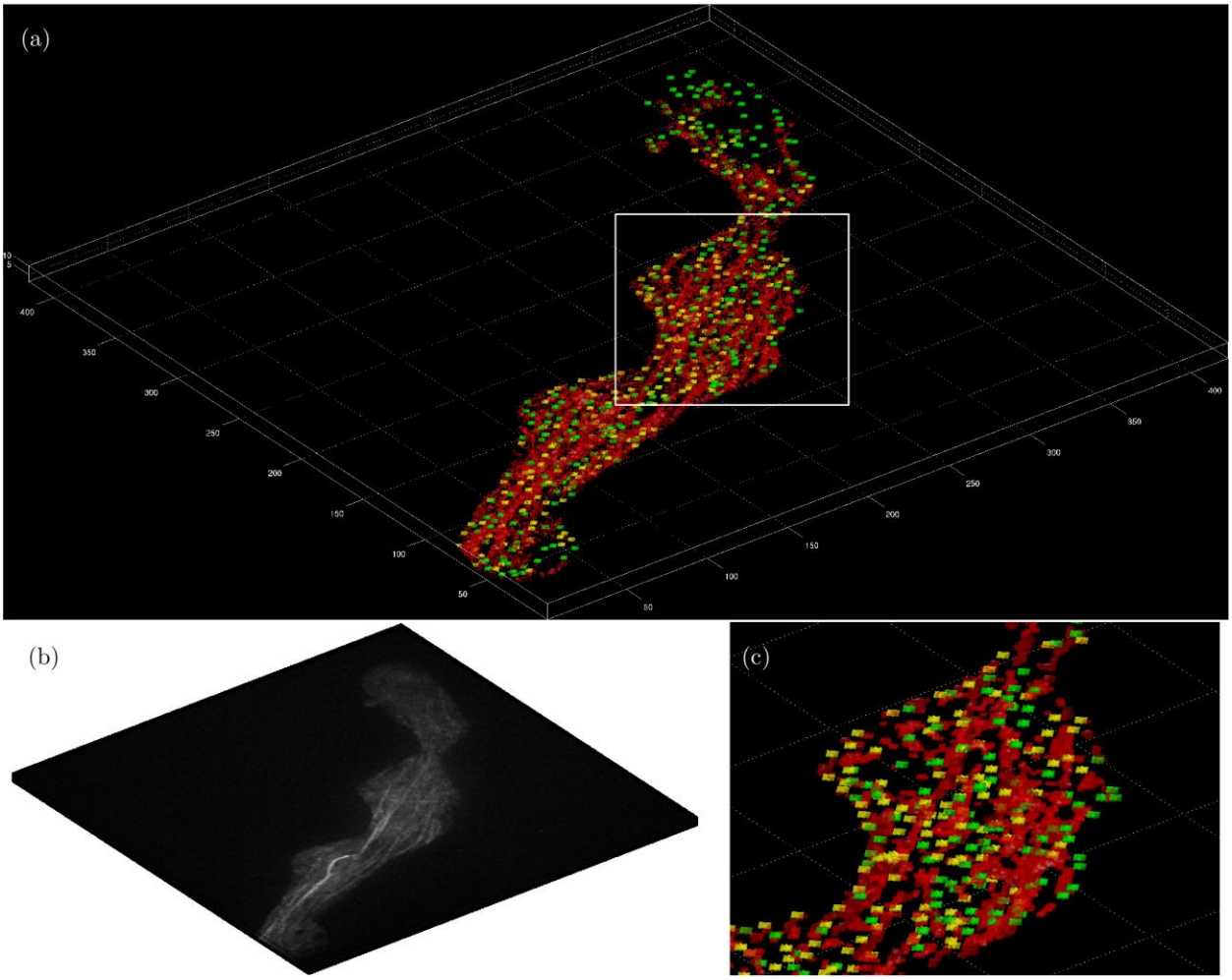

Fig. 6. RFP-FABD2 and MitoTracker label segmentation and colocalisation. (a) An example of segmentation from a single time point; the image has been rotated to give the best view and the pollen tube tip is at the top of the image. The image shows actin cables (red) and mitochondria (green) as detected by their respective probes. Mitochondria that have been calculated as colocalising are shown in yellow. Mitochondrial size is artificial to make them easier to see. (b) A maximum z projection of RFP-FABD2 label at the same time point. The projection has been rotated such that it matches the segmentation rotation. (c) Shows a zoom of the region highlighted by the white box in (a).

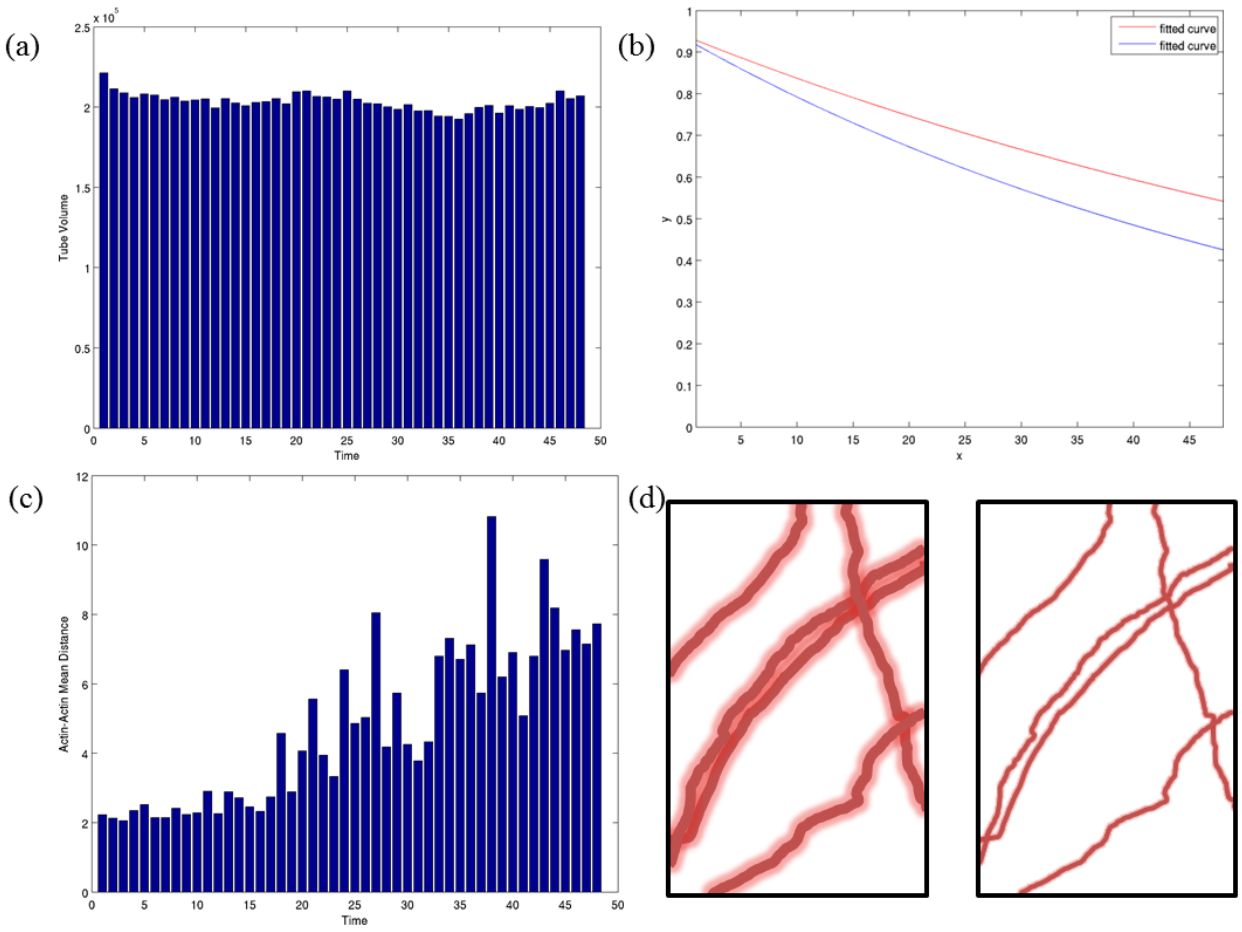

Fig. 7. Bleaching artefacts affect the amount of actin that can be identified by the program. (a) The identifiable pollen tube volume stays the same for all 48 frames; the expectation is that the volume of actin within the tube would stay the same or increase due to more filaments forming thick cables. (b) The volume of actin cables within the pollen tube decreases with time (fitted exponential curve; red); this drop is exponential in nature and follows a similar curve to the drop in average intensity within the pollen tube (fitted exponential curve; blue). The less rapid decrease in the volume of actin compared to the mean intensity within the pollen tube is likely due to the Gaussian spread of light during the imaging process and the cube nature of the volume measurement. (c) Decrease in segmented actin volume is balanced by an increased mean actin-actin distance; this implies that detected actin cables appear thinner and that the effect of bleaching may be the detection of thinner actin cables over the loss of actin cable number. (d) A schematic of detected actin cables at an early and late time within the same region of the pollen tube showing how bleaching can lead to a decrease in thickness of the actin and the Gaussian blur around the actin signals.

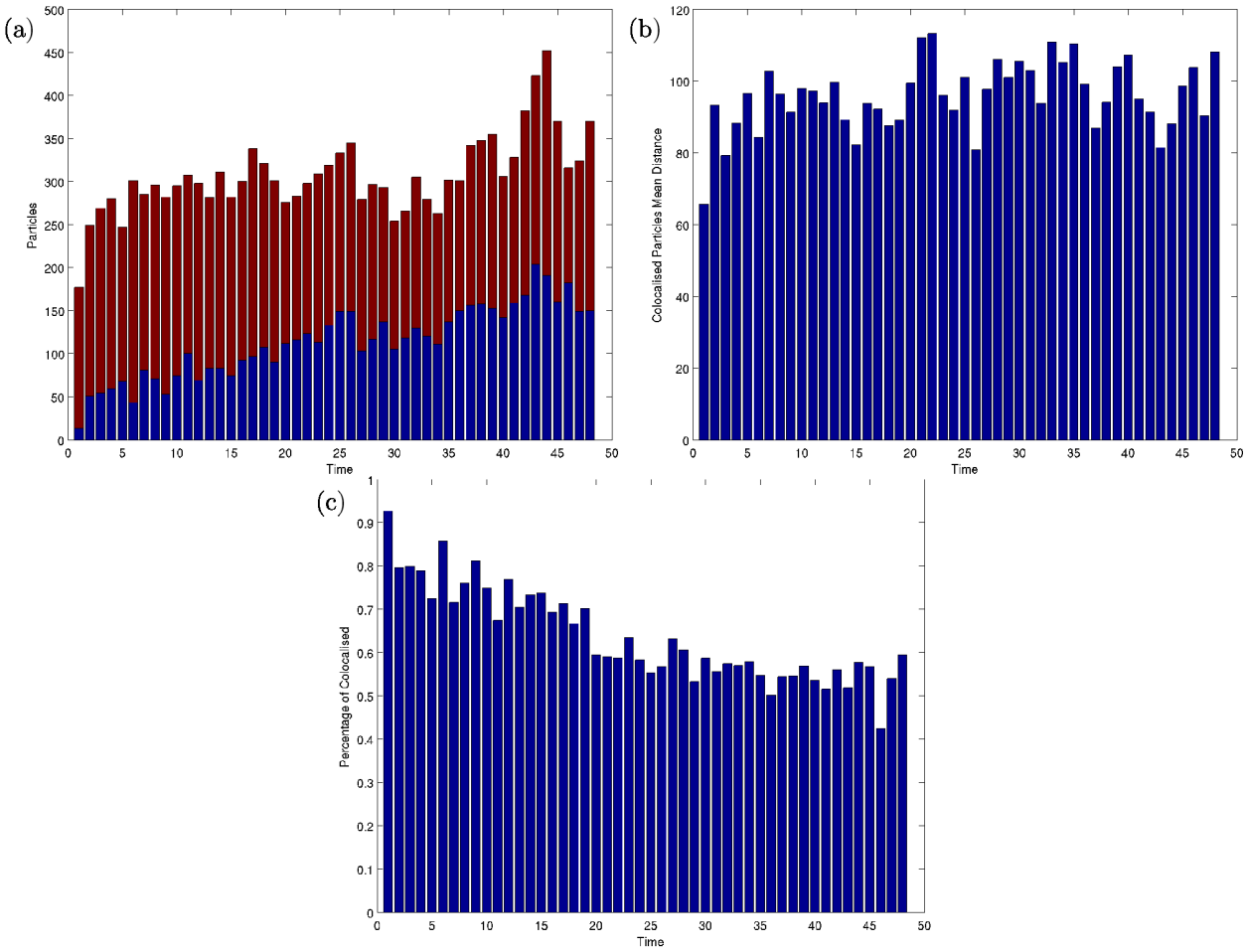

Fig. 8. Colocalisation of mitochondria with actin is successfully assessed despite bleaching. (a) Number of mitochondria 'particles' detected at each time point; the red portion of the bar shows the colocalised mitochondria, the blue portion the non-colocalised. (b) The mean distance between colocalising mitochondria and actin signals vary between frames; however, if bleaching was creating false positives we would expect to see an exponential increase that mirrors the exponential decrease in intensity due to brightness. Note that the percentage of colocalising mitochondria decreases with time; this could be due to an increase in total number of recognised MitoTracker signals or, which fits the data (not shown), an increase in false positives due to bleaching of the actin channel. (c) The percentage of colocalising mitochondria decreases with time. The pattern of decrease may match the bleaching issues identified for actin segmentation; it is likely that some mitochondria are considered too far from segmentable actin due to the bleaching effects on the program. This decrease in identified Mitotracker signals is not due to an increase in mitochondria in regions where actin filaments are sub-resolution and unsegmentable.

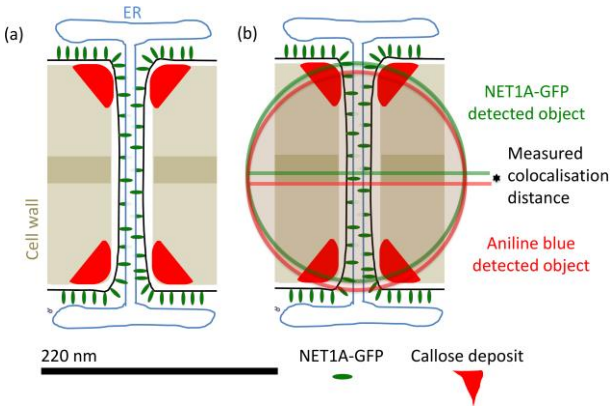

Fig. 9. Diagrams showing the relative positioning of some molecular components of *Arabidopsis thaliana* root meristem plasmodesmata. Cell wall and channel width are drawn to approximate scale. (a) Arrangement of plasmodesmata as suggested by transmission electron microscopy and light microscopy (e.g. Deeks et al. 2012). (b) In this perfectly symmetrical scenario the centroid positions for callose and NET1A-GFP would be perfectly aligned. The signal for NET1A-GFP (green ring) would overlap almost entirely the signal for aniline blue (callose deposit) in the cell wall.